Journal of Materials Chemistry C

ROYAL SOCIETY OF CHEMISTRY

PAPER

View Article Online
View Journal | View Issue

Cite this: J. Mater. Chem. C, 2024, 12, 4013

Evaluation of vanadium coordination compounds derived from simple acetic acid hydrazide as non-conventional semiconductors†

Josipa Sarjanović, [a] Edi Topić, [a] Mirta Rubčić, [a] Lidija Androš Dubraja, [b] Luka Pavić *[b] and Jana Pisk *[a]

Received 30th January 2024,
Accepted 17th February 2024

DOI: 10.1039/d4tc00433g

rsc.li/materials-c

Vanadium hydrazone complexes were prepared by the reaction of $[VO(C_5H_7O_2)_2]$ and NH_4VO_3 with hydrazone ligands. The ligands were prepared by the reaction of acetic acid hydrazide with 2-hydroxy-5-nitrobenzaldehyde ($\mathbf{H_2L^1}$), 2-hydroxybenzaldehyde ($\mathbf{H_2L^2}$), or 2-hydroxy-3-methoxybenzaldehyde ($\mathbf{H_2L^3}$). Mononuclear and dinuclear vanadium(v) complexes were characterized by spectroscopic methods and elemental analysis, while their thermal behaviour was examined by thermogravimetry and temperature-dependent powder X-ray diffraction. The structural transformations of specific complexes were observed by applying the *in situ* solid-state impedance spectroscopy (SS-IS) technique, and their electrical characteristics were systematically correlated with their thermal and structural properties. Crystal and molecular structures of complexes $(NH_4)[VO_2(L^1)]$, $[VO(L^1)(OMe)(MeOH)]$, $[VO(L^2)(OMe)(MeOH)]\cdot MeOH$, $[VO(L^3)(OMe)(MeOH)]$, $[VO(L^3)(OEt)(H_2O)]$, and $[VO_2(HL^3)]_2\cdot 2H_2O$, were determined by single crystal X-ray diffraction and their optical properties were assessed using UV-Vis diffuse reflectance spectroscopy.

Introduction

Although a plethora of vanadium coordination compounds and their diverse applications are documented, the exploration of their electrical and dielectric properties, along with their potential application as semiconductors, remains an enigmatic and underexplored domain.[1–4] Existing literature abounds with intricate vanadium compounds synthesized through reactions of vanadium with various hydrazone ligands, frequently employing aroyl-hydrazones. The utility of hydrazones as ligands is underscored by their facile synthesis and the presence of multiple donor atoms, oxygen (O), nitrogen (N), and occasionally sulphur (S). These systems exhibit adaptability during coordination and protonation/deprotonation processes tailored to the oxidation state of the metal, thereby expanding the array of feasible complexes attainable under distinct synthetic conditions, such as solvent choice, co-ligand variations with differing donor atom counts, stoichiometry, substrate diversity, and atmospheric conditions (aerobic/anaerobic), among others.

Frequently reported, complexes formed by hydrazone-based ligands with transition metal ions have demonstrated heightened antimicrobial activity.[5–11] In that regard, Cu complexes containing ligands obtained by the reaction of acetic acid hydrazide and *o*-vanillin were reported.[12,13] On the other hand, there is a limited availability of complex compounds with vanadium, that are synthesized from straightforward hydrazones, particularly acyl-hydrazones.[14–20] Therefore, the focal point of our research endeavours pertained to generating vanadium coordination complexes through reactions with hydrazones, which are derivatives of acetic acid hydrazide. Due to this, three different aldehydes, 2-hydroxybenzaldehyde, 2-hydroxy-3-methoxybenzaldehyde, and 2-hydroxy-5-nitrobenzaldehyde (Fig. 1), were utilized to create hydrazones, to discern the impact of substituents on the benzene ring of the ligand on the characteristics of the resulting vanadium complex (Scheme 1 and ESI,† Scheme S1).

Furthermore, electrical conductivity is an outcome of electron or ion movement, contingent upon the material's composition and structure and can be studied by impedance spectroscopy (IS).[21–24] A distinction exists between ionic and electronic conductivity.[25–27] In ionic conductivity, the charge carriers comprise ions, and conductivity hinges on ion concentration and mobility, while electrons govern electronic conductivity as charge carriers. Charge transfer, particularly evident in organic compounds, is a prominent mechanism elucidating

[a] Department of Chemistry, Faculty of Science, University of Zagreb, Horvatovac 102a, Zagreb, Croatia. E-mail: jana.pisk@chem.pmf.hr
[b] Ruđer Bošković Institute, Bijenička cesta 54, Zagreb, Croatia. E-mail: lpavic@irb.hr

† Electronic supplementary information (ESI) available. CCDC 2306364–2306369. For ESI and crystallographic data in CIF or other electronic format see DOI: https://doi.org/10.1039/d4tc00433g

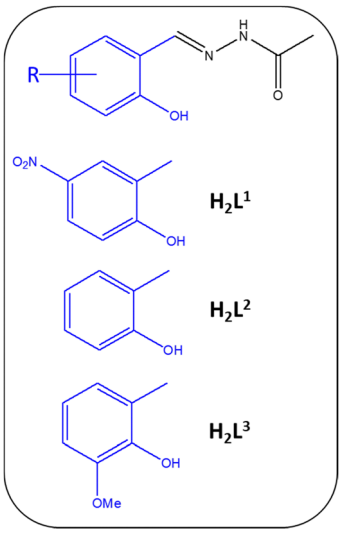

Fig. 1 Ligands used for the presented investigation.

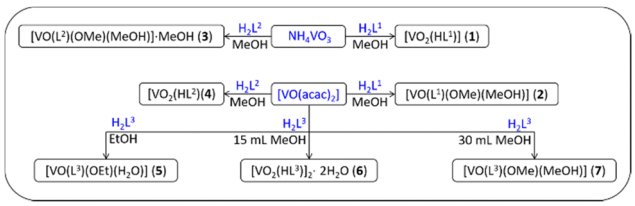

Scheme 1 General scheme and abbreviations used for the prepared vanadium complexes. Blue compounds were used as starting precursors.

electronic conductivity. In the case of ligand-to-metal charge-transfer (LMCT),[28–32] the transfer occurs *via* electrons from donor atoms of the ligand, notably oxygen (O) and nitrogen (N), to the metal centre, which acts as the electron acceptor. In conjugated systems, π electrons exhibit mobility, manifesting semiconducting behaviour characterized by increasing conductivity with rising temperature.[33]

Electrical properties of complexes comprising transition metals such as Cu(II), Co(II), and Hg(II), in conjunction with Schiff base ligands embedded in plastic PVC membranes, have been employed to craft highly selective thiocyanate electrodes.[34]

Moreover, impedance spectroscopy has been utilized to investigate the mechanism governing selectivity towards SCN^-, while the dielectric properties and conductivity of azine complexes involving Co(II), Cu(II), Ni(II), and Cd(II),[35] along with complexes of Co(II), Ni(II), and Cu(II) derived from aldehyde derivatives and glycine dipeptide, have been reported in the literature.[36] Additionally, recent studies have delved into the dielectric properties and conductivity of complexes of Co(II), Cu(II), and Ni(II) with ligands synthesized through reactions involving Schiff bases.[37] Notably, references in the literature regarding vanadium complexes emphasize the insufficient exploration of their electrical and dielectric properties. For instance, vanadium complexes with tetradentate Schiff bases[38] and vanadium indanone derivatives[39] exhibit semiconductor characteristics which can be further employed in the manufacturing of electronic gadgets such as light-emitting diodes, rechargeable batteries, sensors, and electronic devices. Moreover, the electrical and magnetic properties of vanadium(IV) complex compounds prepared through reactions with aroylhydrazone ligands have been explored. A recently published study has presented results on the synthesis and characterization of molybdenum complexes with hydrazone ligands, derivatives of 2-hydroxybenzhydrazide, and 4-hydroxybenzhydrazide.[40] The study also encompassed an in-depth examination of the *in situ* transformation of these complex compounds using solid-state impedance spectroscopy.

Considering the aforementioned reasons, the primary objective of our research is to conduct an in-depth investigation into the electrical properties of the prepared vanadium complex compounds. This investigation employs the *in situ* SS-IS method, encompassing a wide range of frequencies and temperatures, to elucidate how potential structural alterations, contingent on temperature fluctuations, impact electrical conductivity. Given the underexplored realm of these complexes as semiconductors in existing literature, this study seeks to contribute new insights that will advance the understanding of this class of materials. In this context, the optical properties of materials containing vanadium were investigated and compared to insights reported in the literature. Furthermore, we aim to demonstrate the sensitivity of the SS-IS method in monitoring structural changes and transformations, aligning the results of electrical property analysis with those of thermal and structural assessments.

Results and discussion

Preparation and characterization of vanadium complexes

The preparative route for the ligand H_2L^3 was not previously reported and the ligand was obtained by the condensation reaction of 2-hydroxy-3-methoxybenzaldehyde and acetic acid hydrazide (ratio 1 : 1, in methanol). The IR spectrum of the ligand has a characteristic C=O band at 1672 cm^{-1}, while the band at 1609 cm^{-1} corresponds to the stretching of the C=N bond, characteristic of Schiff bases (Fig. S1, ESI†). DSC analysis (ESI,† Fig. S2) showed that the compound is stable up to 180 °C followed by an endothermic minimum attributed to the melting process. There are no other minima present on the curve, which means that both reactants have reacted completely.

The reactions of the prepared ligands H_2L^{1-3} with the starting compounds of vanadium [$VO(C_5H_7O_2)_2$] and NH_4VO_3 were carried out in different solvents (methanol and ethanol), in a molar ratio of 1 : 1. The reaction of NH_4VO_3 and H_2L^1, in methanol, provided a mononuclear complex (NH_4)[$VO_2(L^1)$] (**1**). The same complex was also obtained by the direct *in situ* reaction of NH_4VO_3, aldehyde, and hydrazide, either in methanol or ethanol. When NH_4VO_3 was substituted by [$VO(acac)_2$] as vanadium precursor, in methanol, a new complex [$VO(L^1)$]-(OMe)(MeOH)] (**2**) was isolated. In both cases, the H_2L^1 ligand is coordinated to the metal centre *via* the ONO atom, as indicated by the IR spectra (Fig. S3 and S4, ESI†) with bands

at 1330 cm^{-1} ($(NH_4)[VO_2(L^1)]$) (**1**) and 1341 cm^{-1} ($[VO(L^1)(OMe)(MeOH)]$) (**2**), attributed to stretching of the C–O group of the hydrazone moiety. The bands at 1612 cm^{-1} ($(NH_4)[VO_2(L^1)]$) (**1**) and 1599 cm^{-1} ($[VO(L^1)(OMe)(MeOH)]$) (**2**) correspond to the C═N (imine) group. Also, bands at 1248 cm^{-1} ($(NH_4)[VO_2(L^1)]$) (**1**) and 1299 cm^{-1} ($[VO(L^1)(OMe)(MeOH)]$) (**2**) characteristic for C–O phenyl group stretching were observed. There are bands at 918 cm^{-1} and 906 cm^{-1} ($(NH_4)[VO_2(L^1)]$) (**1**) and 967 cm^{-1} ($[VO(L^1)(OMe)(MeOH)]$) (**2**) corresponding to the stretching of the V═O group (Fig. S3 and S4, ESI†). When the mononuclear complex compound ($(NH_4)[VO_2(L^1)]$) (**1**) is heated in an oxygen atmosphere, a decrease in the mass is present in one step, from 224 °C to 441 °C (ESI,† Fig. S9), which corresponds to the decomposition of the complex. The final orange product after thermal analysis was identified as V_2O_5, which was confirmed by comparing the IR-ATR spectra of the residue and the previously prepared vanadium(v) oxide. As an additional confirmation, the diffractogram of the product powder after thermal analysis and the prepared vanadium(v) oxide were compared. Furthermore, thermogravimetric analysis of the mononuclear compound $[VO(L^1)(OMe)(MeOH)]$ (**2**) also observed a one-step decomposition in the temperature range from 106 °C to 424 °C (Fig. S10, ESI†). On the TG curve, it is not possible to distinguish the loss of the coordinated solvent molecule from the beginning of the decomposition, but on the DSC curve, the endothermic signal at 120 °C could indicate the loss of the methanol molecule. Analysing the PXRD diffractogram of the mononuclear complex $[VO(L^1)(OMe)(MeOH)]$ (**2**), it was observed that above 160 °C, the complex $[VO(L^1)(OMe)(MeOH)]$ (**2**) turns potentially into a mononuclear complex $[VO_2(HL^1)]$.[19]

By the reaction of NH_4VO_3 and H_2L^2, in methanol, several monocrystals were isolated, and identified as mononuclear complex $[VO(L^2)(OMe)(MeOH)]\cdot MeOH$ (**3**). The complex is unstable and quickly loses the crystalline and coordinated solvent molecule of the solvent, methanol, and turns into the complex $[VO_2(HL^2)]$ (**4**). The above was confirmed by comparing the IR spectra of the sample obtained by the reaction of H_2L^2 with NH_4VO_3 and H_2L^2 with $[VO(acac)_2]$ in methanol. IR analysis (Fig. S5, ESI†) showed a band at 1341 cm^{-1}, which corresponds to stretching of the C–O group of the hydrazone part, a band at 1613 cm^{-1} belonging to the C═N (imine) group, and a band at 1276 cm^{-1} characteristic of stretching C–O phenyl groups. At 976 cm^{-1} band characteristic of the stretching of the V═O group was observed. The decomposition of the mononuclear complex $[VO_2(HL^2)]$ (**4**) occurs in one step, as seen from the thermogram (Fig. S11, ESI†), which starts at 186 °C and ends at 538 °C. The mononuclear compound $[VO_2(HL^2)]$ (**4**) was previously reported in the CCDC database (refcode FUNNIO),[19] however, in this research, different vanadium starting compounds, solvents, and reaction time were used for its preparation. In the previously published publication, the synthesis was carried out by reacting NH_4VO_3 with the ligand H_2L^2 in dimethylformamide, with a reflux of five hours, while in this work, the synthesis was carried out for two hours, using a more environmentally friendly solvent, methanol. By the reaction of H_2L^3 with $[VO(acac)_2]$, in a ratio of 1 : 1, in ethanol, mononuclear complex $[VO(L^3)(OEt)(H_2O)]$ (**5**) was obtained. Using methanol as a solvent made it possible to isolate two different complex compounds, depending on the concentration of the solution, *i.e.*, the volume of methanol and the mass of the reactants used. A dinuclear complex $[VO_2(HL^3)]_2\cdot 2H_2O$ (**6**) was formed from a more concentrated solution (15 mL methanol), and a mononuclear complex $[VO(L_3)(OMe)(MeOH)]$ (**7**) was isolated from a more dilute solution (30 mL methanol). As in the previous complexes, the ligand is bounded to the metal centre *via* the ONO atom, while the vanadium is hexa-coordinated. Characteristic bands for these compounds were determined by IR analysis and compared to the literature.[19,41,42] The band at 1339 cm^{-1} $[VO(L^3)(OEt)(H_2O)]$ (**5**), 1332 cm^{-1} $[VO_2(HL^3)]_2\cdot 2H_2O$ (**6**) and 1351 cm^{-1} $[VO(L^3)(OMe)(MeOH)]$ (**7**) corresponds to the stretching of the C–O group of the ligand, while the band at 1620 cm^{-1} $[VO(L^3)(OEt)(H_2O)]$ (**5**), 1574 cm^{-1} $[VO_2(HL^3)]_2\cdot 2H_2O$ (**6**) and 1611 cm^{-1} $[VO(L^3)(OMe)(MeOH)]$ (**7**) belongs to the stretching of the C═N bond of the ligand group. Also, a band was observed at 1259 cm^{-1} $[VO(L^3)(OEt)(H_2O)]$ (**5**), 1251 cm^{-1} $[VO_2(HL^3)]_2\cdot 2H_2O$ (**6**) and 1256 cm^{-1} $[VO(L^3)(OMe)(MeOH)]$ (**7**) characteristic for the stretching of the C–O group. The band present at 964 cm^{-1} for $[VO(L^3)(OEt)(H_2O)]$ (**5**), 920 cm^{-1} and 851 cm^{-1} for $[VO_2(HL^3)]_2\cdot 2H_2O$ (**6**) and 957 cm^{-1} $[VO(L^3)(OMe)(MeOH)]$ (**7**) indicates stretching of the V═O group (Fig. S6–S8, ESI†). In the case of the mononuclear complex compound $[VO(L^3)(OMe)(MeOH)]$ (**7**) at 1032 cm^{-1}, a MeOH stretching band was observed.

Thermogravimetric analysis was performed for complexes obtained from H_2L^3 ligand (Fig. S12–S14, ESI†), Table 1. The mononuclear complex $[VO(L^3)(OEt)(H_2O)]$ (**5**) and the dinuclear complex $[VO_2(L^3)]_2\cdot 2H_2O$ (**6**) show decomposition in one wide step, in which individual steps cannot be differentiated. For the mononuclear complex $[VO(L^3)(OEt)(H_2O)]$ (**5**), decomposition occurs in a wide temperature range of 85–517 °C, and for the dinuclear complex $[VO_2(HL^3)]_2\cdot 2H_2O$ (**6**) in the range 48–506 °C. In the case of the mononuclear compound $[VO(L^3)(OMe)(MeOH)]$ (**7**), the decomposition of the complex takes place in two steps. The first step takes place from 70 °C to 102 °C and corresponds to the elimination of the coordinated methanol molecule from the mononuclear complex. The second step refers to the decomposition of the complex and takes place between 195–512 °C.

Ultimately, seven different vanadium coordination complexes were prepared, and the synthetic routes are shown in Scheme S1 (ESI†). Although, based on the experimental data,

Table 1 Thermal analysis of obtained V(v) complexes

Vanadium complexes	Complex decomposition temperatures/°C	Coordinated solvent loss/°C
$(NH_4)[VO_2(L^1)]$ (**1**)	224–441	—
$[VO(L^1)(OMe)(MeOH)]$ (**2**)	106–424	N.d.
$[VO_2(HL^2)]$ (**4**)	186–538	—
$[VO(L^3)(OEt)(H_2O)]$ (**5**)	85–517	N.d.
$[VO_2(HL^3)]_2\cdot 2H_2O$ (**6**)	48–506	—
$[VO(L^3)(OMe)(MeOH)]$ (**7**)	195–512	70–102

N.d. could not be clearly defined.

no concrete conclusion can be made about the preferred product that will be formed by a certain synthetic route, it can be assumed that the reaction $[VO(acac)_2]$ with a ligand prepared from the simplest aldehyde, 2-hydroxybenzaldehyde, the expected product will be of the type $[VO_2(HL)]$, and in reactions with ligands prepared from substituted 2-hydroxybenzaldehyde, products of the general formula [VOL(D)(OR)] will be formed, where ROH is alcohol and D is a water or alcohol molecule. The most unexpected product of the entire research is the dinuclear complex $[VO_2(HL^3)]_2{\cdot}2H_2O$, which is formed from a concentrated methanol solution by prolonged standing.

Description of molecular and crystal structures

SCXRD. In the $[VO(L^2)(OMe)(MeOH)]{\cdot}MeOH$ (**3**) (ESI,† Scheme S1 and Tables S1, S2) vanadium atom achieves a distorted octahedral coordination environment that is realized by attachment of $(L^1)^{2-}$ ion in a tridentate O, N,O fashion and coordination of auxiliary methoxo unit and a methanol molecule. In this complex the $(L^1)^{2-}$ ion coordinates in its hydrazidato tautomeric form (ESI,† Scheme S2) which is evident from the relevant bond lengths.[43,44] The packing of molecules in the solid state is dictated by the presence of non-coordinated methanol molecules, which connect complexes *via* O–H···O and O–H···N hydrogen bonds with the $R_4^4(14)$ motif into supramolecular dimers which further associate in the crystal structure *via* C–H···O interactions (ESI,† Fig. S15). In $[VO(L^3)(OEt)(H_2O)]$ (**5**) (Fig. 2) one observes a similar scenario as in $[VO(L^2)(OMe)(MeOH)]$ (**3**), as can be seen from the related bond distances (ESI,† Table S3). Namely, the ligand coordinates to the VO^{3+} core as dianion in its hydrazidato tautomeric form *via* ONO donor atoms.[42,43] Here as well vanadium(v) is found in a distorted octahedral environment that is realized through the coordination of an ethoxo moiety ensemble through O–H···N, O–H···O and C–H···O hydrogen bonds into complexes 3D architectures (ESI,† Fig. S16).

In $(NH_4)[VO_2(L^1)]$ (**1**) (ESI,† Scheme S1,) the ligand coordinates to the VO_2^+ core as dianion in the hydrazidato tautomeric form through ONO donor atoms,[19] thus affording complex anion where vanadium(v) achieves a distorted square-pyramidal environment. In the crystal structure ammonium cations and complex anions connect through a plethora of N–H···N, N–H···O and C–H···O hydrogen bonds into an intricate supramolecular network (ESI,† Table S4 and Fig. S17).

$[VO(L^1)(OMe)(MeOH)]$ (**2**) (ESI,† Scheme S1) crystallizes with two molecules in the asymmetric unit. The structure of this complex is comparable with that of the $[VO(L^2)(OMe)(MeOH)]$ (**3**) (ESI,† Scheme S1). Namely, the complex displays the distorted octahedral geometry with the L^{2-} ion coordinated in the hydrazidato tautomeric form *via* ONO donor atoms,[43,44] along with a methoxo moiety and a methanol molecule. In the crystal structure molecules associate into complex O–H···N and C–H···O hydrogen-bonded network (ESI,† Table S5 and Fig. S18).

The $[VO_2(HL^3)]_2{\cdot}2H_2O$ (**6**) (Fig. 3) has a dimeric structure, in which the two ligands bind to separate VO^{3+} units as monoanions of the hydrazonato tautomer *via* ONO donor atoms.[19] Octahedral environment around each vanadium atom is completed through the coordination of two bridging oxo anions. The water molecules present in the crystal structure allow the formation of N–H···O, O–H···O, and C–H···O hydrogen-bonded layers in the *ac*-plane which then further assemble through van der Waals interactions into three-dimensional architecture (ESI,† Table S6 and Fig. S19, S20).

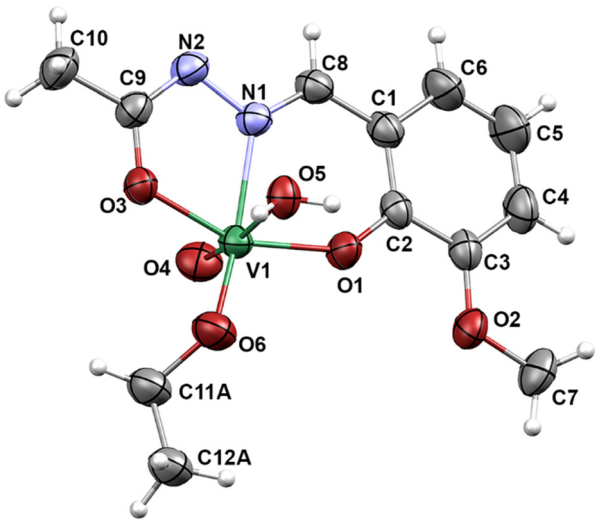

Fig. 2 Molecular structure of $[VO(L^3)(OEt)(H_2O)]$ (**5**). The displacement ellipsoids are drawn at 30% probability level at 298 K. Hydrogen atoms are presented as spheres of arbitrary small radii.

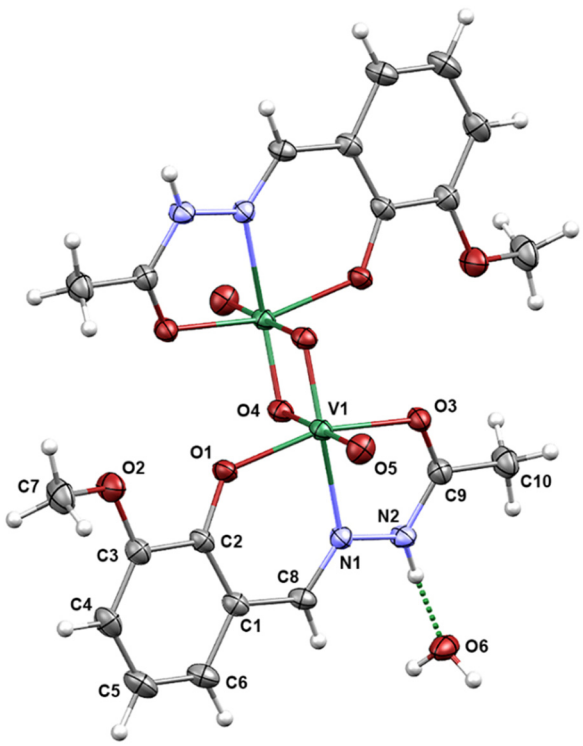

Fig. 3 Molecular structure of $[VO_2(HL^3)]_2{\cdot}2H_2O$ (**6**). The displacement ellipsoids are drawn at 30% probability level at 298 K. Hydrogen atoms are presented as spheres of arbitrary small radii.

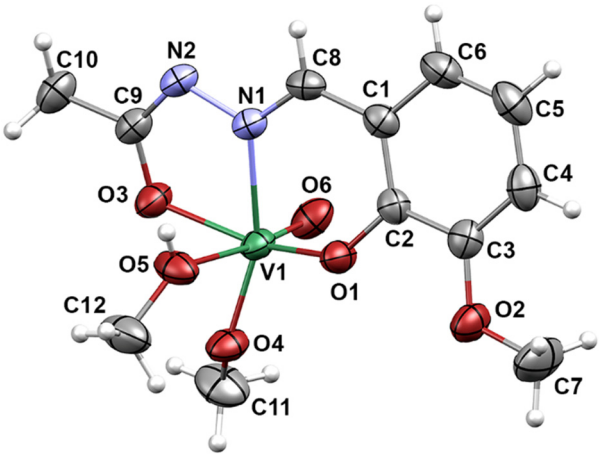

Fig. 4 Molecular structure of [VO(L^3)(OMe)(MeOH)] (**7**). The displacement ellipsoids are drawn at 30% probability level at 298 K. Hydrogen atoms are presented as spheres of arbitrary small radii.

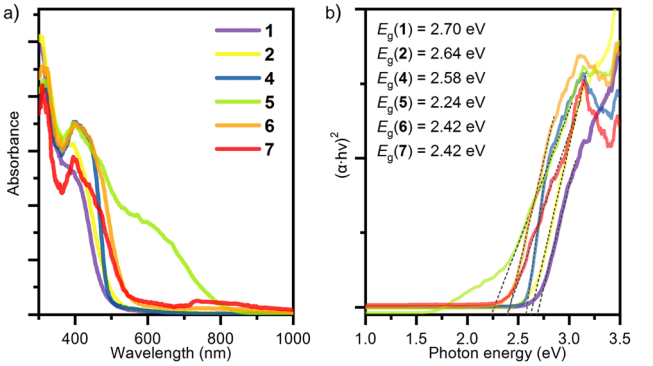

Fig. 5 (a) Kubelka–Munk diffuse reflectance absorption spectrum of compounds $(NH_4)[VO_2(L^1)]$ (**1**), $[VO(L^1)(OMe)(MeOH)]$ (**2**), $[VO_2(HL^2)]$ (**4**) $[VO(L^3)(OEt)(H_2O)]$ (**5**), $[VO_2(HL^3)]_2{\cdot}2H_2O$ (**6**) and $[VO(L^3)(OMe)(MeOH)]$ (**7**); and (b) direct optical transitions. Dashed lines indicate the band gap energies.

$[VO(L^3)(OMe)(MeOH)]$ (**7**) (Fig. 4) has a molecular structure quite similar to that of $[VO(L^2)(OMe)(MeOH)]$ (**3**). Here as well complex displays the distorted octahedral geometry with the L^{2-} ion coordinated in the hydrazidato tautomeric form *via* ONO donor atoms,[43,44] alongside a methoxo moiety and a methanol molecule. Complexes form through O–H···N hydrogen bonds of the $R_2^2(10)$ motif supramolecular dimers that further associate *via* C–H···O interactions in the crystal structure (ESI,† Table S7 and Fig. S21). The structure of $[VO_2(HL^2)]$ (**4**) has been previously reported and here the ligand binds in the monoanionic form of the hydrazonato tautomer through ONO donor atoms.[19]

Optical properties of the obtained vanadium complexes

The optical properties of complexes $(NH_4)[VO_2(L^1)]$ (**1**), $[VO(L^1)(OMe)(MeOH)]$ (**2**), $[VO_2(HL^2)]$ (**4**), $[VO(L^3)(OEt)(H_2O)]$ (**5**), $[VO_2(HL^3)]_2{\cdot}2H_2O$ (**6**) and $[VO(L^3)(OMe)(MeOH)]$ (**7**) in the solid state were analysed by UV-Vis diffuse reflectance spectroscopy, at room temperature. All complexes exhibit vanadium in the 5+ oxidation state and show strong absorption at the edge of the visible spectrum (Fig. 5), which is due to the presence of the LMCT-based d^0 chromophore.[45] In complexes $(NH_4)[VO_2(L^1)]$ (**1**) and $[VO_2(HL^2)]$ (**4**), vanadium is located in a distorted square-pyramidal environment, while complexes $[VO(L^1)(OMe)(MeOH)]$ (**2**), $[VO(L^3)(OEt)(H_2O)]$ (**5**) $[VO_2(HL^3)]_2{\cdot}2H_2O$ (**6**) and $[VO(L^3)(OMe)(MeOH)]$ (**7**) exhibit a distorted octahedral geometry. The fact that all studied complexes have one nitrogen donor atom and four or five oxygen donor atoms coordinated to vanadium is responsible for only minor differences in the spectra, which are dominated by the LMCT transitions. In agreement with the similarities in the diffuse reflectance spectra, the complexes exhibit an optical band gap in the range of 2.24–2.70 eV. These values are characteristic of wide-bandgap semiconductors and are in fair agreement with other literature reports for compounds with vanadium(v) in an octahedral environment and O-donor ligands.[46,47] The band gap energy of V_2O_5, for example, in which vanadium(v) is surrounded by six oxygen atoms, was found to directly allow a transition of 2.3 eV, according to both experimental and theoretical calculations.[48,49]

PXRD. The temperature-dependent PXRD data (ESI,† Fig. S22–S26) was utilized to unravel the relationships between isolated complexes and their thermal degradation products. All crystalline phases observed in the diffraction patterns were successfully modelled using Rietveld fit with crystal structure models where available (ESI,† Fig. S27–S30), or using le Bail with a plausible unit cell found by indexation routine (ESI,† Fig. S31–S34). For each sample, unit cell and complex molar volume as functions of temperature were analysed. The results confirm the stark contrast between the thermal behaviour of prepared complexes. $[VO(L^1)(OMe)(MeOH)]$ (**2**) (Fig. 6 and ESI,† Fig. S10, S23, S28) is relatively stable up to 110 °C, where it loses both methanol molecules simultaneously, yielding an intermediate phase. Further heating results in additional molar volume change and conversion, to presumably, $[VO_2(HL^1)]$, as previously observed for a similar complex.[19] On the other hand, $(NH_4)[VO_2(L^1)]$ (**1**) is stable up to 160 °C (ESI,† Fig. S9, S22, S27), when it also converts to $[VO_2(HL^1)]$ or isomorphous phase, followed by insignificant molar volume change above the conversion temperature. Likewise, $[VO_2(HL^2)]$ (**4**) is stable up to 180 °C (ESI,† Fig. S29), and upon further heating becomes amorphous, owing to complex decomposition (ESI,† Fig. S28). On the other hand, complexes derived from H_2L^3 show significantly lower thermal stability. $[VO(L^3)(OMe)(MeOH)]$ (**7**) converts to a degraded complex above 60 °C, which, by considering the unit cell parameters from indexation (ESI,† Fig. S26, S30) and TGA analysis (ESI,† Fig. S14), contains one methanol molecule less per metal atom than its parent compound. At higher temperatures, the degraded complex becomes amorphous. Finally, $[VO(L^3)(OEt)(H_2O)]$ (**5**) becomes fully amorphous above 90 °C (ESI,† Fig. S25), which follows the observed complex decomposition in TGA data (ESI,† Fig. S12).

Impedance spectroscopy measurements

The electrical properties of vanadium complexes, prepared from methanol and ethanol, were studied using the method

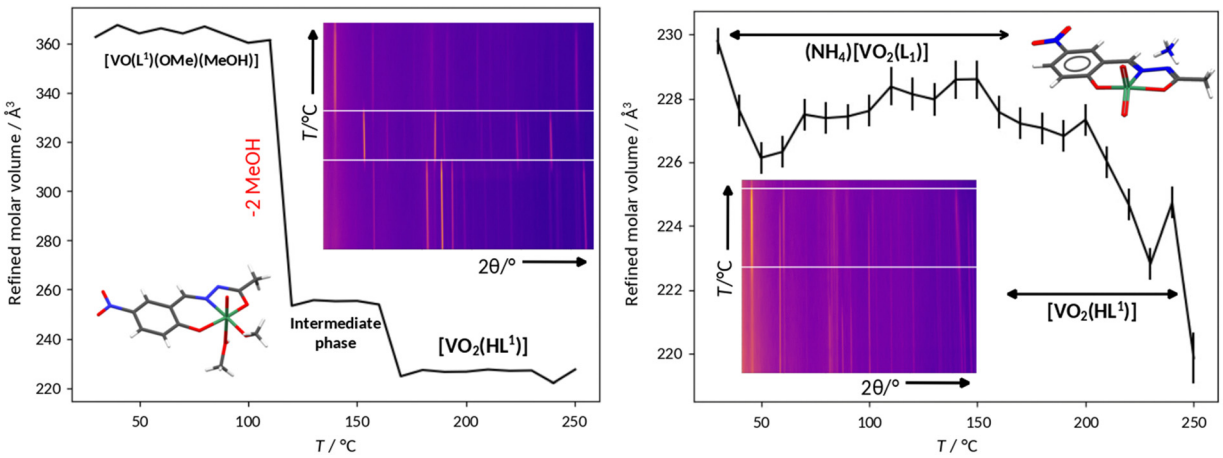

Fig. 6 Left: Temperature-dependent PXRD data (inset) and analysis of [VO(L^1)(OMe)(MeOH)] (**2**). Phase transformations occur at around 110 °C and 160 °C. Based on the change of molar volume, the compound transforms to an intermediate phase by loss of two methanol molecules per molecule of complex and then converts to, presumably, fully desolvated complex [VO_2(HL^1)].[19] Right: Temperature-dependent PXRD data (inset) and analysis of (NH_4)[VO_2(L^1)]. A phase transformation occurs at around 160 °C, yielding a phase with pattern identical to one of [VO_2(HL^1)] as observed in decomposition of [VO(L^1)(OMe)(MeOH)] (**2**).

of solid-state impedance spectroscopy (SS-IS). Five mononuclear complexes were analysed: (NH_4)[VO_2(L^1)] (**1**), [VO(L^1)(OMe)(MeOH)] (**2**), [VO_2(HL^2)] (**4**), [VO(L^3)(OEt)(H_2O)] (**5**) and [VO(L^3)(OMe)(MeOH)] (**7**) and one dinuclear complex [VO_2(HL^3)]$_2$·2H_2O (**6**). Since the results of the thermal analysis most often show the decomposition of the complex in a wide temperature range, *i.e.* it is not possible to unambiguously determine the loss of the solvent, decoordination of the solvent and the decomposition of the complex itself, temperature-dependent diffractograms were additionally recorded for complexes (NH_4)[VO_2(L^1)] (**1**), [VO(L^1)(OMe)(MeOH)] (**2**), [VO_2(HL^2)] (**4**), [VO(L^3)(OEt)(H_2O)] (**5**) and [VO(L^3)(OMe)(MeOH)] (**7**) (Fig. S22–S26, ESI†).

Based on the results of TGA and PXRD, the temperature range of impedance spectroscopy recording was selected. A heating and cooling cycle was followed, with a step of 20 °C: heating took place from 20 °C to 200 °C/230 °C, and then cooling back to 20 °C. The maximum temperatures of 200 °C and 230 °C were chosen because heating at these temperatures allows the complete elimination of solvent molecules and either retention of the transformed crystalline products or sample amorphization.

The frequency dependence of the real part of the electrical conductivity, σ', *i.e.* the conductivity spectrum for the sample (NH_4)[VO_2(L^1)] (**1**), is shown in Fig. 7. It is obvious that electrical conductivity increases with increasing temperature. All investigated compounds show similar temperature behaviour and behave as semiconductors. Moreover, at high temperatures and low frequencies, the conductivity does not show frequency dependence with a corresponding independent part (the so-called DC plateau). In the area of high frequencies, the conductivity depends on the frequency and is related to the alternating conductivity (dispersion part – AC). The transition from DC to the dispersion region moves towards higher frequencies with increasing temperature. Due to the low conductivity of investigated complexes at lower temperatures, the DC value cannot be determined by direct reading from the graph. The specified value should be calculated by analysing the experimental spectra of the complex impedance by modelling the electrical equivalent circuit (EEC), using the complex nonlinear least square method (complex nonlinear least square – CNLS), see Experimental section, materials and methods.

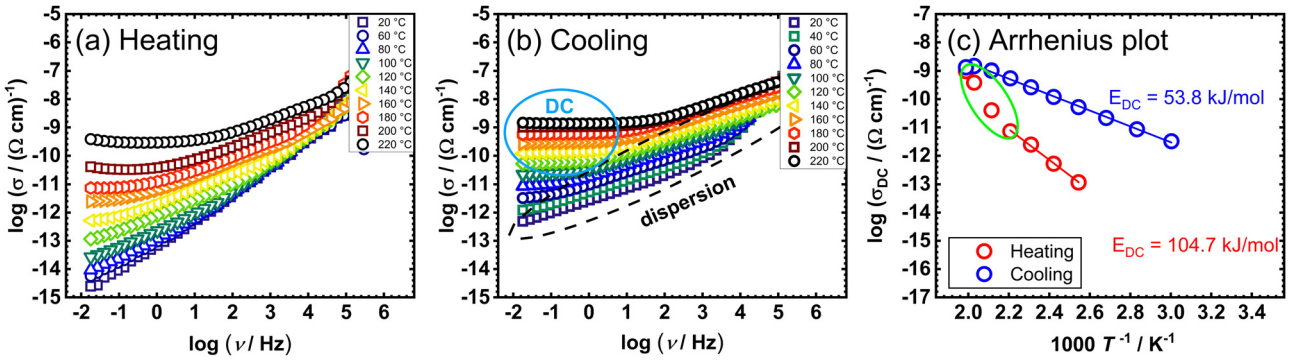

Fig. 7 Conductivity spectra for mononuclear (NH_4)[VO_2(L^1)] sample (complex 1) in heating (a) and cooling (b) runs, and (c) temperature dependence of DC conductivity (log(σ_{DC}) *vs.* 1000/*T*) for both runs (red circle—heating, blue circle—cooling).

For all studied complexes, the impedance spectrum contains a single semicircle related to the bulk effects (see ESI,† Fig. S35 and S36). This is characteristic of electronic conductors, so a simplified EEC model (R-CPE) is used for modelling. The obtained capacitance values for the observed process fall within the range of 10^{-11}–10^{-12} F and are associated with the bulk effect. Furthermore, parameter α is in the range 0.7–0.95 which is in line with the level of semicircle depression and deviation of the ideal capacitor, which implies that studied complexes show a combined nature and behave as resistor and capacitor.

From the conductivity spectra in the heating and cooling cycle, a change in temperature behaviour can be observed for the mentioned $(NH_4)[VO_2(L^1)]$ (**1**) Fig. 7. In the heating cycle, a monotonic change in conductivity is observed (conductivity increases with increasing temperature) up to approximately 180 °C, which is consistent with the thermogram and the temperature-dependent diffractogram (ESI,† Fig. S9 and S22).

However, with further heating, there is a non-monotonic change with increasing temperature, *i.e.* a sudden jump in conductivity in the temperature range between 180–230 °C, Fig. 7(a), which is consistent with the onset of decomposition visible in the TG curve above 220 °C (ESI,† Fig. S9). Impedance spectroscopy confirmed that the mononuclear complex $(NH_4)[VO_2(L^1)]$ (**1**) has a one-step decomposition, which is consistent with PXRD and TG analysis, however, the decomposition was observed at slightly lower temperatures. The mentioned effect points to the sensitivity of the impedance spectroscopy method, and the possibility of monitoring *in situ* small changes in the structure that have an impact on the electrical characteristics of the investigated complex. On the other hand, in the cooling cycle, there is a monotonous change in conductivity with temperature change, Fig. 7(b) and (c).

The DC conductivity exhibits Arrhenius temperature dependence for all complexes and has characteristic activation energy, Fig. 7(c). Given that the studied sample $(NH_4)[VO_2(L^1)]$ (**1**) shows a temperature dependence, Fig. 7(c), it is possible to determine the characteristic activation energy. The activation energy for DC conductivity, E_{DC}, for each complex is determined from the slope of $\log(\sigma_{DC})$ *vs.* $1000/T$ using the equation: $\sigma_{DC} = \sigma_0^* \exp(-E_{DC}/k_B T)$ where σ_{DC} is the DC conductivity, σ_0^* is the pre-exponent, k_B is the Boltzmann constant, and T is the temperature (K). The activation energy, E_{DC}, for all investigated complexes, are listed in Table 2.

A linear dependence of DC conductivity on temperature ($1000/T$) was observed in the heating cycle up to 180 °C, and in the cooling cycle in the entire temperature range, with a change in the slope of the direction. In the heating cycle, before the transformation of complex $(NH_4)[VO_2(L^1)]$ (**1**) the activation energy is 104.7 kJ mol^{-1}, while after transformation the activation energy drops to 53.8 kJ mol^{-1}. The mentioned transformation is accompanied by an increase in conductivity throughout the entire temperature range, for example almost 3 orders of magnitude at 120 °C in the heating and cooling cycle (1.1×10^{-13} *vs.* 5.2×10^{-11} (Ω cm)$^{-1}$).

Furthermore, the IS analysis for the mononuclear compound $[VO(L^1)(OMe)(MeOH)]$ (**2**) is shown in ESI,† Fig. S37.

Table 2 Activation energy values for DC conductivity, E_{DC}, of synthesized vanadium complexes. H and C denote the heating and cooling runs, respectively

Vanadium complex	Run	E_{DC}/kJ mol^{-1}
$(NH_4)[VO_2(L^1)]$ (**1**)	H	104.7
$(NH_4)[VO_2(L^1)]$ (**1**)	C	53.8
$[VO(L^1)(OMe)(MeOH)]$ (**2**)	C	54.2
$[VO_2(HL^2)]$ (**4**)	C	75.4
$[VO(L^3)(OEt)(H_2O)]$ (**5**)	H	190.3
$[VO(L^3)(OMe)(MeOH)]$ (7)	C	66.8
$[VO_2(HL^3)]_2{\cdot}2H_2O$ (**6**)	C	67.6

During the heating (heating cycle) of $[VO(L^1)(OMe)(MeOH)]$ (**2**), the first non-monotonic change was observed at a temperature of ∼100–120 °C, which is followed by a monotonous jump between the curves and remains continuous up to ∼180 °C. After 180 °C, a small non-monotonic change (jump in conductivity) is observed again, ESI,† Fig. S37(a).

The obtained results are in accordance with the TGA and PXRD analysis of the mononuclear complex $[VO(L^1)(OMe)(MeOH)]$ (**2**). Up to 100 °C, the mentioned complex $[VO(L^1)(OMe)(MeOH)]$ (**2**) in the conductivity spectrum and the Arrhenius dependence of the DC conductivity, shows a weak temperature dependence. At a temperature of ∼120 °C, the coordinated solvent leaves the molecule (ESI,† Fig. S10 and S23), and the mentioned change in the IS spectrum of conductivity can be observed in the temperature range of 100–160 °C, while at temperatures higher than 170 °C the analyzed complex $[VO(L^1)(OMe)(MeOH)]$ (**2**) turns into the transformed complex $[VO_2(HL^1)]$ (after heating). In the cooling cycle, we do not observe non-monotonic changes, *i.e.* jumps in conductivity values, ESI,† Fig. S37(c), which indicates that the connection remains stable. Based on the temperature dependence, the activation energy in the cooling cycle can be calculated, and the activation energy amounts to 54.2 kJ mol^{-1} and the conductivity @120 °C is 2.1×10^{-11} (Ω cm)$^{-1}$. The obtained activation energy and conductivity values indicate that the transformation of complex $[VO(L^1)(OMe)(MeOH)]$ (**2**), resulted in a complex identical to $(NH_4)[VO_2(L^1)]$ (**1**) after heating (Fig. 7 and ESI,† Fig. S37).

The mononuclear complex $[VO_2(HL^2)]$ (**4**) (ESI,† Fig. S38), was also tested for electrical properties in the heating and cooling cycle.

During heating, the temperature dependence of the conductivity is achieved only after 120 °C, and there are no other significant changes. Such a result is expected, given that the mononuclear complex $[VO_2(HL^2)]$ (**4**) has no coordinated or crystalline solvent in the structure. However, a small change is observed in the interval 160–200 °C, which is consistent with the PXRD (ESI,† Fig. S24) analysis, which points to amorphization of the sample at temperatures above 185 °C. In the cooling process, there is a linear dependence without sudden changes in conductivity, which indicates that the compound remains stable. The calculated activation energy for the transformed mononuclear complex $[VO_2(HL^2)]$, after it becomes amorphous, is 75.4 kJ mol^{-1}.

Furthermore, the mononuclear complex $[VO(L^3)(OEt)(H_2O)]$ (**5**), shows a pronounced temperature dependence of conductivity

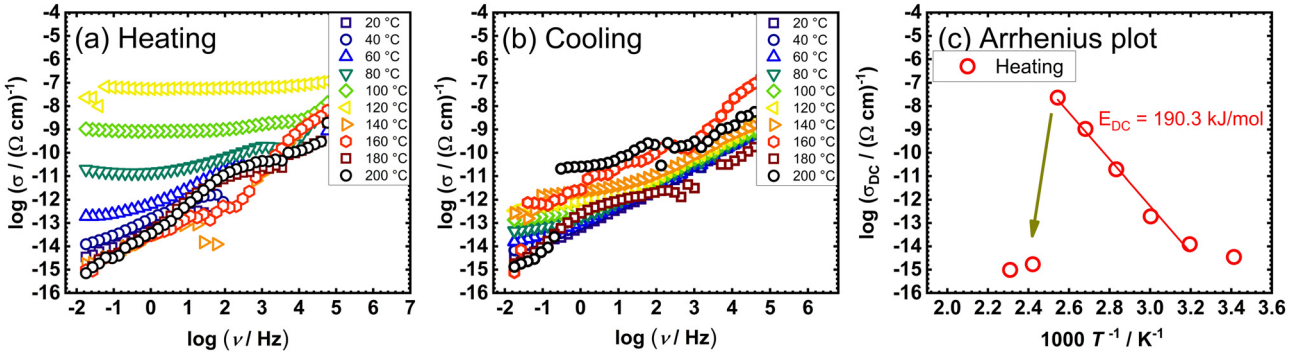

Fig. 8 Conductivity spectra for mononuclear [VO(L^3)(OEt)(H_2O)] sample (complex **5**) in heating (a) and cooling (b) runs, and (c) temperature dependence of DC conductivity (log(σ_{DC}) *vs.* 1000/*T*) for both runs (red circle – heating, blue circle – cooling).

up to 120 °C, (Fig. 8). Above this temperature, there is a sudden drop in conductivity, and electrical contact is lost, which indicates the decomposition of the sample. PXRD analysis at a temperature of 110 °C shows the amorphization of the sample and then the decomposition of the mononuclear complex [VO(L^3)(OEt)(H_2O)] (**5**), which is in agreement with the electrical measurements. For the mentioned sample, the activation energy can be calculated, Fig. 8(c), in the heating cycle, before decomposition, and is 190.3 kJ mol^{-1}. The obtained high value of activation energy, and at the same time high conductivity (2.32×10^{-8} (Ω cm)$^{-1}$@ 120 °C) is very interesting and will be the subject of further research.

The last mononuclear sample analysed by the SS-IS method is [VO(L^3)(OMe)(MeOH)] (**7**) (ESI,† Fig. S39). In the temperature-dependent PXRD, ESI,† Fig. S26, a change of the complex was observed at 60 °C due to the loss of coordinated methanol, and at a temperature above 150 °C the compound becomes amorphous. By processing the data of the heating cycle of the mononuclear complex [VO(L^3)(OMe)(MeOH)] (**7**), a sudden non-monotonic jump in conductivity between temperatures 140 °C–170 °C was observed. This jump confirmed the change in the structure of the complex, *i.e.* the amorphization of [VO(L^3)-(OMe)(MeOH)] (**7**). The change at 60 °C, which corresponds to the release of solvent, is not visible in the SS-IS results, which can be attributed to low conductivity and low sensitivity at low temperatures. In the cooling cycle, the transformed complex is stable, a linear dependence was observed, and the activation energy of complex [VO(L^3)(OMe)(MeOH)] (**7**) was calculated to be 66.8 kJ mol^{-1}.

One dinuclear complex [VO_2(HL^3)]$_2$·2H_2O (**6**) was also investigated using the IS method. The results are shown in Fig. 9. By analysing the heating cycle of dinuclear complex [VO_2(HL^3)]$_2$·2H_2O (**6**), it was observed that below 100 °C the conductivity shows a weak temperature dependence. In contrast, in the temperature interval from 100 °C to 140 °C there are two large jumps in conductivity values and non-monotonic changes.

Analysis of the DSC curve in that area indicates an endothermic minimum that could correspond to the release of a water molecule from the structure of the analysed dinuclear [VO_2(HL^3)]$_2$·2H_2O (**6**). At temperatures above 160 °C, there is a weak but visible drop in the conductivity of the complex, which points to the decomposition of the initial complex followed by amorphization of the sample. In the cooling cycle, there are no significant changes in the conductivity of the initial complex after the transformation, and the activation energy was determined to be 67.6 kJ mol^{-1}. For a clearer comparison, Table 2 shows the activation energies for all six analysed complexes, complexes (NH_4)[VO_2(L^1)] (**1**), [VO(L^1)(OMe)(MeOH)] (**2**), [VO_2(HL^2)] (**4**), [VO(L^3)(OMe)(MeOH)] (**7**) and [VO_2(HL^3)]$_2$·2H_2O (**6**) in the cooling cycle, and complexes (NH_4)[VO_2(L^1)] (**1**) and [VO(L^3)(OEt)(H_2O)] (**5**) in the heating cycle. Complex (NH_4)[VO_2(L^1)]

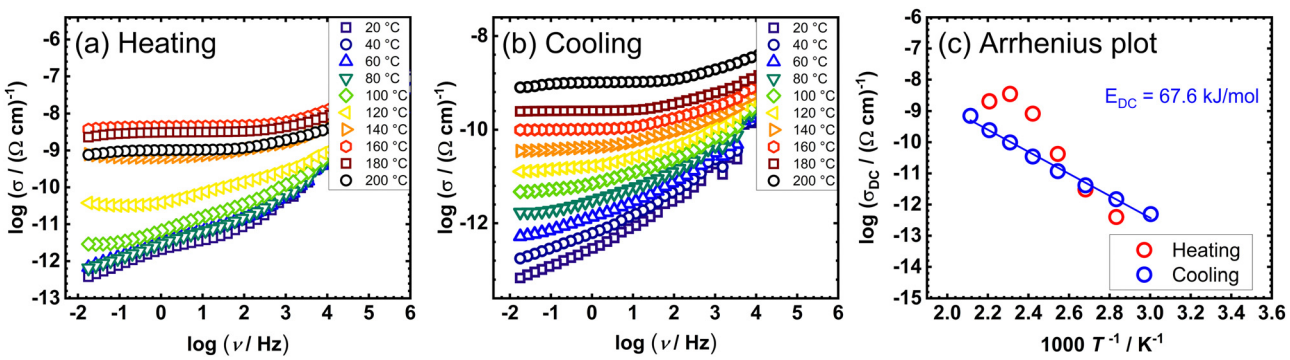

Fig. 9 Conductivity spectra for dinuclear [VO_2(L^3)]$_2$·2H_2O sample (complex **6**) in heating (a) and cooling (b) runs, and (c) temperature dependence of DC conductivity (log(σ_{DC}) *vs.* 1000/*T*) for both runs (red circle – heating, blue circle – cooling).

(**1**) before amorphization shows an energy of ~92 kJ mol^{-1}. After amorphization, the energy drops to ~54 kJ mol^{-1}, which is a positive effect and the compound becomes more conductive by up to three orders of magnitude. A similar value of activation energy and conductivity was observed for complexes $(NH_4)[VO_2(L^1)]$ (**1**) and $[VO(L^1)(OMe)(MeOH)]$ (**2**) after transformation, which indicates that complex $[VO(L^1)(OMe)(MeOH)]$ (**2**) potentially changes to complex $[VO_2(HL^1)]$ upon heating. A higher activation energy than the others is visible for mononuclear complex $[VO_2(HL^2)]$ (**4**) after transformation (75 *vs.* 54 kJ mol^{-1}). The reason could be that there are no substituents (–NO_2 or –OMe groups) on the benzene ring of the ligand. In the other two ligands, we find additional groups attached to the benzene ring (H_2L^1–NO_2, H_2L^3–OCH_3), which can be assumed to affect the activation energy and conductivity.

Furthermore, the obtained high value of activation energy ~190 kJ mol^{-1}, and at the same time high conductivity (~1×10^{-7} $(\Omega\ cm)^{-1}$) for complex $[VO(L^3)(OEt)(H_2O)]$ (**5**) before decomposition (up to 120 °C), is an extremely interesting feature and will be the subject of further research. It can be assumed that the high value of conductivity can be attributed to the amorphization of the sample that occurs at the lowest temperature (in comparison to other investigated samples). Mononuclear complex $[VO(L^3)(OMe)(MeOH)]$ (**7**) and dinuclear complex $[VO_2(HL^3)]_2{\cdot}2H_2O$ (**6**) after transformation have similar activation energy (66 *vs.* 67 kJ mol^{-1}), presuming the transformation into analogue species during the process of heating, as for the complexes $(NH_4)[VO_2(L^1)]$ (**1**) and $[VO(L^1)(OMe)(MeOH)]$ (**2**). It is also interesting to note that the dinuclear complex $[VO_2(HL^3)]_2{\cdot}2H_2O$ (**6**) shows an order of magnitude higher conductivity (~10^{-9} *vs.* 10^{-10} $(\Omega\ cm)^{-1}$). Also, the difference between complex $(NH_4)[VO_2(L^1)]$ (**1**) which has the highest conductivity, and complex $[VO(L^3)(OMe)(MeOH)]$ (**7**), which has the lowest conductivity, amounts to almost two orders of magnitude (1.09×10^{-9} *vs.* 5.60×10^{-11} $(\Omega\ cm)^{-1}$). In addition to the above, the subject of further research will be to examine the influence of substituents on the benzene ring of the ligand, as well as the transformation process itself and the influence on the electrical properties of vanadium complexes.

Experimental

Synthetic procedures

The following chemicals were used without additional purification: 2-hydroxy-3-methoxy benzaldehyde 99%, AlfaAesar, Acetic acid hydrazide 95%, Acros Organics, Ammonium mono vanadate, p.a. MERCK – ALKALOID, Methanol, p.a. Gram-mol, Ethanol, CARLO ERBA REAGENTS. The following compounds were prepared by literature procedures: oxobis(pentane-2,4-dionato)vanadium(IV), (*E*)-*N*′-[(2-hydroxy-5-nitrophenyl)methylene]acetohydrazide (H_2L^1), (*E*)-*N*′-(2-hydroxybenzylidene)acetohydrazide (H_2L^2).

Ligand synthesis

H_2L^3. Yellow 2-hydroxy-3-methoxybenzalaldehyde (0.5163 g, 3.394 mmol) was dissolved in 30 mL of methanol in a 100 mL round flask. White acetic acid hydrazide (0.2512 g, 3.394 mmol) was added to the colourless solution. The reaction was prepared in a 1 : 1 ratio and was refluxed for two hours and left at room temperature. The resulting white crystals were separated by filtration and analysed using IR-ATR, DSC analysis and X-ray diffraction on a single crystal.

Solution synthesis: white crystals, 0.5909 g were obtained with a yield of 83.6%.

IR-ATR: ν/cm^{-1}: 3317 and 3185 ν O–H, 2939 ν C–H (CH_3), 2868 ν_{as} C–H (CH_2), 2838 ν_s C–H (CH_2), 1672 ν C=O (ketone), 1609 C=N (imine).

DSC: T_e = 179.98 °C, E = 33.24 kJ mol^{-1}.

Synthesis of mononuclear complexes

$(NH_4)[VO_2(L^1)]$ (1). In a 100 mL round flask, the ligand H_2L^1 (20.00 mg, 89.56 μmol) was dissolved in 15 mL of methanol. NH_4VO_3 (10.47 mg, 89.56 μmol) was added to the yellow solution. The reaction was prepared in a ratio of 1 : 1 and refluxed for two hours and left until the appearance of a precipitate at room temperature. The precipitate was filtered through a black ribbon without additional washing. The resulting yellow crystals were analysed using IR-ATR spectroscopy, TGA/DSC analysis, X-ray diffraction on a single crystal, temperature-dependent X-ray diffraction on a powder sample and impedance spectroscopy.

Solution synthesis: yellow crystals, 21.08 mg were obtained with a yield of 72.6%.

IR-ATR: ν/cm^{-1}: 2939 ν C–H (CH_3), 1612 C=N (imine), 1248 C–O, 918 i 906 ν V=O.

TGA: w_t (V_2O_5) = 56.48%, w_{exp} (V_2O_5) = 57.22%.

EA: C_t: 33.45, C_{exp}: 34.27, H_t: 3.74, H_{exp}: 3.81, N_t: 17.34, N_{exp}: 17.60.

PXRD: the compound is stable up to 250 °C after it becomes amorphous.

$[VO(L^1)(OMe)(MeOH)]$ (2). In a 100 mL round flask, the ligand H_2L^1 (20.00 mg, 89.56 μmol) was dissolved in 15 mL of methanol. $[VO(acac)_2]$ (23.75 mg, 89.56 μmol) was added to the yellow solution. The reaction was prepared in a ratio of 1 : 1 and refluxed for two hours and left until the appearance of a precipitate at room temperature. The precipitate was filtered through a black ribbon without additional washing. The resulting orange crystals were analysed using IR-ATR spectroscopy, TGA/DSC analysis, X-ray diffraction on a single crystal, temperature-dependent X-ray diffraction on a powder sample and impedance spectroscopy.

Solution synthesis: orange crystals, 20.47 mg were obtained with a yield of 72.9%.

IR-ATR: ν/cm^{-1}: 2940 ν C–H (CH_3), 1599 C=N (imin), 1299 C–O, 967 ν V=O.

TGA: w_t (V_2O_5) = 59.96%, w_{exp} (V_2O_5,) = 56.86%.

EA: C_t: 37.62, C_{exp}: 37.29, H_t: 4.02, H_{exp}: 3.90, N_t: 11.97, N_{exp}: 11.54.

PXRD: phases were detected: 20–115 °C phase 1, 115–165 °C phase 2, 165–250 °C phase 3.

$[VO(L^2)(OMe)(MeOH)]{\cdot}MeOH$ (3). In a 100 mL round flask, the ligand H_2L^2 (20.00 mg, 112.79 μmol) was dissolved in 15 mL of methanol. NH_4VO^3 (13.19 mg, 112.79 μmol) was added to the

colourless solution. The reaction was prepared in a ratio of 1 : 1 and refluxed for two hours and left until the appearance of only a few single crystals at room temperature. The resulting orange crystals were analysed using single-crystal X-ray diffraction.

Solution synthesis: orange crystals, 0.40 mg were obtained with a yield of 1%.

$[VO_2(HL^2)]$ (4). The ligand H_2L^2 (20.00 mg, 112.75 μmol) was dissolved in 15 mL of methanol or ethanol in a 100 mL round flask. $[VO(acac)_2]$ (29.91 mg, 112.75 μmol) was added to the colourless solution. The reaction was prepared in a ratio of 1 : 1 and refluxed for two hours and left until the appearance of a precipitate at room temperature. The precipitate was filtered through a black ribbon without additional washing. The resulting yellow crystals were analysed using IR-ATR spectroscopy, TGA/DSC analysis, X-ray diffraction on a single crystal, temperature-dependent X-ray diffraction on a powder sample and impedance spectroscopy.

Complex compound **4** can also be obtained by the synthesis of NH_3VO_4 with H_2L^2 in ethanol.

Solution synthesis: orange crystals, 20.69 g were obtained with a yield of 70.6%.

IR-ATR: ν/cm^{-1}:2932 ν C–H (CH_3), 2904 ν C–H (CH_2), 1613 C═N (imine), 1276 C–O, 1032 ν MeOH, 971 ν V═O.

TGA: w_t (V_2O_5) = 65.86%, w_{exp} (V_2O_5) = 68.02%.

EA: C_t: 41.56, C_{exp}: 41,03, H_t: 3.49, H_{exp}: 3.65, N_t: 10.77, N_{exp}: 10.23.

PXRD: the compound is stable up to 185 °C after it becomes amorphous.

$[VO(L^3)(OEt)(H_2O)]$ (5). In a 100 mL round flask, the ligand H_2L^3 (20.00 mg, 96.00 μmol) was dissolved in 15 mL of ethanol. $[VO(acac)_2]$ (25.46 mg, 96.00 μmol) was added to the colourless solution. The reaction was prepared in a ratio of 1 : 1 and refluxed for two hours and left until the appearance of a precipitate at room temperature. The precipitate was filtered through a black ribbon without additional washing. The resulting brown crystals were analysed using IR-ATR spectroscopy, TGA/DSC analysis, X-ray diffraction on a single crystal, temperature-dependent X-ray diffraction on a powder sample and impedance spectroscopy.

Complex compound 5 can also be obtained by the synthesis of NH_3VO_4 with H_2L^3 in ethanol.

Solution synthesis: orange-brown crystals, 24.88 mg were obtained with a yield of 76.6%.

IR-ATR: ν/cm^{-1}: 2929 ν C–H (CH_3), 2892 ν C–H (CH_2), 1620 C═N (imine), 1259 C–O, 1042 ν MeOH, 964 ν V═O.

TGA: w_t (V_2O_5) = 54.24%, w_{exp} (V_2O_5,) = 52.96%.

EA: C_t: 42.87, C_{exp}: 42.12, H_t: 5.10, H_{exp}: 5.35, N_t: 8.33, N_{exp}: 8.02.

PXRD: the compound is stable up to 110 °C after it becomes amorphous.

$[VO(L^3)(OMe)(MeOH)]$ (7). In a 100 mL round flask, the ligand H_2L^3 (60.00 mg, 288.00 μmol) was dissolved in 30 mL of methanol. $[VO(acac)_2]$ (76.38 mg, 288.00 μmol) was added to the colourless solution. The reaction was prepared in a ratio of 1 : 1 and refluxed for two hours and left until the appearance of a precipitate at room temperature. The precipitate was filtered through a black ribbon without additional washing. The resulting brown crystals were analysed using IR-ATR spectroscopy, TGA/DSC analysis, X-ray diffraction on a single crystal, temperature-dependent X-ray diffraction on a powder sample and impedance spectroscopy.

Solution synthesis: brown crystals, 86.40 mg were obtained with a yield of 81.1%.

IR-ATR: ν/cm^{-1}: 2949 ν C–H (CH_3), 2905 ν C–H (CH_2), 1611 C═N (imine), 1256 C–O, 1032 ν MeOH, 957 ν V═O.

TGA: w_t (MeOH) = 8.65%, w_{exp} (MeOH) = 9.95%, w_t (V_2O_5) = 53.8%, w_{exp} (V_2O_5) = 51.2%.

EA: C_t: 42.87, C_{exp}: 42.21 H_t: 5.10, H_{exp}: 5.31, N_t: 8.33, N_{exp}: 8.42.

Synthesis of dinuclear complex

$[VO_2(HL^3)]_2{\cdot}2H_2O$ (6). In a 100 mL round flask, the ligand H_2L^3 (20.00 mg, 96.00 μmol) was dissolved in 15 mL of methanol. $[VO(acac)_2]$ (25.46 mg, 96.00 μmol) was added to the colourless solution. The reaction was prepared in a ratio of 1 : 1 and refluxed for two hours and left until the appearance of a precipitate at room temperature. The precipitate was filtered through a black ribbon without additional washing. The resulting orange crystals were analysed using IR-ATR spectroscopy, TGA/DSC analysis, single crystal X-ray diffraction and impedance spectroscopy.

Solution synthesis: orange crystals, 20.99 mg were obtained with a yield of 72.9%.

IR-ATR: ν/cm^{-1}: 3000 ν C–H (CH_3), 1574 C═N (imine), 1251 C–O, 920 i 851 ν V═O

TGA: w_t (V_2O_5) = 30,39%, w_{exp} (V_2O_5) = 28,74%.

EA: C_t: 40.15, C_{exp}: 40.02, H_t: 4.04, H_{exp}: 4.24, N_t: 9.36, N_{exp}: 9.13.

Materials and methods

The prepared compounds were characterized and identified using elemental analysis (EA), infrared spectroscopy (IR-ATR, infrared spectroscopy – attenuated total reflectance), thermogravimetric analysis (TGA), differential scanning calorimetry (DSC), temperature-dependent X-ray diffraction on a powder sample (PXRD), single crystal X-ray diffraction (SCXRD), UV-Vis diffuse reflectance spectroscopy (DRS) and impedance spectroscopy (IS).

IR-ATR spectroscopic analysis was performed on a PerkinElmer Spectrum Two spectrometer equipped with a diamond ATR attachment. The recording was carried out in the 4000–400 cm^{-1} range with four scans. The spectra were processed and analysed with the Excel program.

Differential scanning calorimetry (DSC) analysis was performed on a Mettler-Toledo DSC823e instrument in the range from 25 °C to 300 °C in an inert nitrogen atmosphere with a flow rate of 50 mL min^{-1} and heating of 10 °C min^{-1}. The samples were recorded in closed aluminium containers. The measurement results were processed with the Mettler STARe Evaluation Software v17.00 program.

Thermogravimetric (TGA) analyses were performed using a Mettler-Toledo TGA/DSC 3+ in closed aluminium oxide

containers. All experiments were performed in an oxygen atmosphere with a flow rate of 200 cm^3 min^{-1} and heating at 10 °C min^{-1}. The recording was carried out in the temperature range from 25 °C to 600 °C. The measurement results were processed with the Mettler STARe Evaluation Software v17.00 program.

UV-Vis diffuse reflectance spectra were recorded at 293 K using a Shimadzu UV-Vis-NIR spectrometer (model UV-3600) equipped with an integrated sphere. Barium sulphate was used as a reference. The diffuse reflectance spectra were transformed using the Kubelka–Munk function. Tauc plots were used to calculate the optical band gap energy.

Complex impedance was measured over a wide range of frequencies (0.01 Hz to 1 MHz) and temperature (20–200 °C, step 20 °C) using an impedance analyser (Novocontrol Alpha-AN dielectric spectrometer). The temperature is controlled to ±0.2 °C. The measurements were performed on powder samples pressed into cylindrical disks with a diameter of 5 mm and a thickness of 1 mm under a uniform load of 2×10^3 kg using a hydraulic press. Gold electrodes with a diameter of 3.8 mm were used for electrical contact, deposited on both sides of the disk using an SC7620 magnetron from Quorum Technologies. The sample is then placed between two electrodes of the BDS cell, top and bottom, in a sandwich configuration. The impedance spectra were analysed by means of equivalent electrical circuits (EEC) modelling and parameters were obtained by the complex non-linear least square (CNLLSQ) fitting. System sample-electrode shows resistance (R) and capacitance (C) related to the sample, connected in a ''sandwich'' configuration, and can be modelled with RC element. For all studied complexes, the impedance spectrum contains a single semicircle related to the bulk effects (see Fig. S35 and S36 ESI†). Preferably, such a semicircular arc passes through the origin of the complex plot and leads to a low-frequency intersection point on the real axis of the complex plot, corresponding to the resistance of the sample. An ideal semicircle is generally not observed, and the complex impedance plots typical for most of the materials as well as for all samples from this study consist of a single depressed semicircle with the center below the real axis, so we use constant-phase element (CPE) rather than the capacitor in the equivalent circuits. The CPE is an empirical function given by: $Z^*_{CPE} = 1/A(j\omega)^{\alpha}$, where A and α are the constants, $0 \leq \alpha \leq 1$, α being 1 for the ideal capacitor, and 0 for the ideal resistor. In a ''rough'' approximation, the parameter A can be equated with the value of the ''real'' capacity. CPEs are commonly employed to better model and represent the impedance of systems that show characteristics such as the spread of relaxation time and inhomogeneity and roughness, or other non-ideal behavior of the sample, which may not be accurately captured by a simple capacitor model. The surface of prepared pellets for electrical characterisation is smooth, and no additional effect is visible in spectra to the addition of a single process observed related to bulk. We did not observe the change in the general spectra shape with temperature, and the overall shape is the same, one semicircle. The only difference is the extent of semicircle formation which is related to temperature and frequency range used in our setup. As temperature increases, semicircle develop and is fully formed at higher temperatures (see ESI,† Fig. S35 and S36) for various complexes studied in this work. From the resistance values obtained from the fitting procedures, and the electrode dimensions (d sample thickness, and A electrode area) the DC conductivity is calculated.

Crystallography

Single crystals of $(NH_4)[VO_2(L^1)]$ (**1**), $[VO(L^1)(OMe)(MeOH)]$ (**2**), $[VO(L^2)(OMe)(MeOH)]\cdot MeOH$ (**3**), $[VO(L^3)(OEt)(H_2O)]$ (**5**), $[VO_2(HL^3)]_2\cdot 2H_2O$ (**6**), $[VO(L^3)(OMe)(MeOH)]$ (**7**) of appropriate quality were selected for the diffraction experiments. Data were compiled using a Rigaku XtaLAB Synergy-S diffractometer equipped with a Dualflex source (Cu Kα radiation, λ = 1.54184 Å) and a HyPix detector. Data were gathered *via* ω-scans at 293 K and data were processed with the CrysAlis program package.[50] A summary of the general crystallographic data is presented in Table S1 (ESI†). The structures were solved by dual-space methods with SHELXT.[51] The refinement was done *via* full-matrix least-squares methods based on F^2 values against all reflections, including the anisotropic displacement parameters for all non-H atoms. Hydrogen atoms attached to carbon atoms were placed in geometrically idealized positions and refined by using the riding model, with $U_{iso} = 1.2U_{eq}$ of the connected carbon atom, or as ideal CH_3 groups, with $U_{iso} = 1.5U_{eq}$. Hydrogen atoms attached to heteroatoms were located in the different Fourier maps in the final stages of the refinement procedure. All refinements were conducted using SHELXL.[52] The SHELX programs were operated within the Olex2 suite.[53] Geometrical calculations were performed by Platon[54] and molecular graphics were produced using Mercury.[55] The structure for $[VO(L^1)(OMe)(MeOH)]$ was solved as a two-component non-merohedral twin, with the two twin domains present in a ratio of 0.3995 : 0.6005. CCDC 2306364–2306369.†

Powder diffraction data were collected on Panalytical Empyrean diffractometer equipped with Cu Kα source with elliptical W/Si focusing mirror and PIXCel3D HPC detector in transmission mode, using Anton Paar TTK 600 sample environment stage. The sample was lightly homogenized before applying it in a thin (0.2 mm) layer on the transmission sample holder between two Kapton sheets. Data were collected in a temperature range from 30 °C to 250 °C in steps of 10 °C, and 2θ range from 5 to 40° in steps of 0.0131°. Heating steps were performed with a heating rate of 1 °C min^{-1}, and the sample was equilibrated for 2 minutes before each measurement. Measurements were done in the air.

Indexing and refinement were done in TOPAS Academic software v.5. Where phase identity was known, starting values of unit cell parameters were chosen to match those from crystal structure data. Unit cell parameters of phases for which crystal structure is not known were chosen based on indexation results and plausible molar volume of the assumed species present in the phase. Background scattering intensities were modelled as a linear combination of Chebyshev polynomials. Instrument-related and sample-related peak convolutions were modelled

using the fundamental parameters approach. All parameters were refined simultaneously with peak intensities.

Conclusions

In the synthesis of vanadium complexes, three distinct ligands characterized by variations in substituent groups on the benzene ring were employed. Seven novel vanadium complex compounds were meticulously prepared from methanol and ethanol and subsequently subjected to comprehensive characterization *via* different analytical techniques. These compounds encompassed the following entities: $(NH_4)[VO_2(L^1)]$ (**1**), $[VO(L^1)(OMe)(MeOH)]$ (**2**), $[VO(L^2)(OMe)(MeOH)]\cdot MeOH$ (**4**), $[VO(L^3)(OEt)(H_2O)]$ (**5**), $[VO_2(HL^3)]_2\cdot 2H_2O$ (**6**), $[VO(L^3)(OMe)(MeOH)]$ (**7**). In all instances, the ligand established coordination with the metal centre through the ONO atom, resulting in penta- or hexa-coordination of vanadium.

Subsequently, six carefully selected complexes underwent thorough scrutiny *via* impedance spectroscopy, which included: $(NH_4)[VO_2(L^1)]$ (**1**), $[VO(L^1)(OMe)(MeOH)]$ (**2**), $[VO_2(HL^2)]$ (**4**), $[VO(L^3)(OEt)(H_2O)]$ (**5**), $[VO_2(HL^3)]_2\cdot 2H_2O$ (**6**) and $[VO(L^3)(OMe)(MeOH)]$ (**7**). Recognizing the intricacy of separating solvent liberation and complex decomposition stages, temperature-dependent diffractograms (PXRD) were captured and correlated to thermogravimetric analysis, affording insight into the optimization of measurements. This involved ascertaining the appropriate heating temperatures for the samples and discerning potential sample alterations.

Impedance spectroscopy was effectively employed to monitor the dynamic *in situ* transformations exhibited by mononuclear and dinuclear complexes. The technique enabled the observation of conductivity variations concurrent with solvent molecule release and sample amorphization, a phenomenon that is not extensively utilized in the context of this specific method. Notably, all examined complexes displayed a temperature-dependent increase in conductivity, exhibiting semiconducting behaviour, along with obtained value of band gap and electronic conductivity which are in line with observed behaviour, aligning with findings from existing literature.

Samples with high conductivity ($(NH_4)[VO_2(L^1)]$ (**1**) – 1.09×10^{-9} $(\Omega\ cm)^{-1}$, $[VO_2(HL^2)]$ (**4**) – 1.00×10^{-9} $(\Omega\ cm)^{-1}$, $[VO(L^3)(OEt)(H_2O)]$ (**5**) – 2.32×10^{-8} $(\Omega\ cm)^{-1}$) and $[VO_2(HL^3)]_2\cdot 2H_2O$ (**6**) – 5.77×10^{-10} $(\Omega\ cm)^{-1}$ demonstrated promising potential for application as semiconductors in diverse electronic devices (*e.g.* light-emitting diodes, rechargeable batteries, sensors, and electronic devices). To further elucidate their utility, it is imperative to delve into the impact of benzene ring substituents on complex stability and, consequently, their conductivity.

Moreover, the horizon of future research beckons the exploration of complexes featuring alternative metal centres such as molybdenum (Mo) or copper (Cu), in conjunction with an expanded array of hydrazone ligands tethered to the vanadium centre. These endeavours hold the promise of expanding the repertoire of multifunctional materials with prospective applications across diverse domains.

Author contributions

Conceptualization: E. T., M. R., L. P., J. P. Data curation: J. S., E. T., M. R., L. A. D., L. P., J. P. Formal analysis: J. S., E. T., M. R., L. A. D., L. P., J. P. Funding acquisition: J. P., L. P. Investigation: J. S., E. T., L. A. D., J. P., L. P. Methodology: E. T., M. R., L. A. D., L. P., J. P. Project administration: J. P., L. P. Resources: E. T., M. R., L. A. D., L. P., J. P. Software: M. R., E. T., L. P. Supervision: M. R., L. P., J. P. Validation: J. S. Visualization: J. S., E. T., M. R., L. A. D., L. P., J. P. Writing – original draft: L. P., J. P. Writing – review & editing: E. T., M. R., L. A. D., L. P., J. P.

Conflicts of interest

There are no conflicts to declare.

Acknowledgements

This work is supported in part by the bilateral project Cogito, no. 49260RA, Sustainable polyesters using Mo and V catalysts. E. T., M. R., and J. P. acknowledge the support of project CIuK (grant KK.01.1.1.02.0016) co-financed by the Croatian Government and the European Union through the European Regional Development Fund-Competitiveness and Cohesion Operational Programme.

References

1 M. Sutradhar, L. M. Martins, M. F. C. G. da Silva and A. J. L. Pombeiro, *Coord. Chem. Rev.*, 2015, **301**, 200.
2 M. Sutradhar, G. Mukherjee, M. G. B. Drew and S. Ghosh, *Inorg. Chem.*, 2006, **45**(13), 5150.
3 D. Dragancea, N. Talmaci, S. Shova, G. Novitchi, D. Darvasiová, P. Rapta, M. Breza, M. S. Galanski, J. Kožíšek, N. M. R. Martins, L. M. D. R. S. Martins, A. J. L. Pombeiro and V. B. Arion, *Inorg. Chem.*, 2016, **55**(18), 9187.
4 M. Rubčić, D. Milić, G. Horvat, I. Đilović, N. Galić, V. Tomišić and M. Cindrić, *Dalton Trans.*, 2009, 9914.
5 S. A. Aboafia, S. A. Elsayed, A. K. A. El–Sayed and A. M. El-Hendawy, *J. Mol. Struct.*, 2018, **39**, 1158.
6 S. Thakur, N. Sarkar, M. G. B. Drew, A. Bauza, A. Frontera and S. Chattopadhyay, *Polyhedron*, 2018, **142**, 83.
7 S. Y. Ebrahimipour, I. Sheikhshoaie, J. Simpson, H. Ebrahimnejad, M. Dusek, N. Kharazmi and V. Eigner, *New J. Chem.*, 2016, **40**, 2401.
8 W. A. Zoubi, F. Kandii and K. Chebani, *Phys. Sci. Res. Int.*, 2014, **2**, 12.
9 W. Cao, Y. Liu, T. Zhang and J. Jia, *Polyhedron*, 2018, **147**, 62.
10 J. R. Anacona and M. Rincones, *Spectrochim. Acta, Part A*, 2015, **141**, 169.
11 S. A. Aly and S. K. Fathalla, *Arabian J. Chem.*, 2020, **13**, 3735.
12 O. Diouf, M. Gaye, D. G. Sall, A. S. Sall, Y. Pontillon and A. Caneschi, *Bull. Chem. Soc. Ethiop.*, 2006, **20**, 35.
13 S. Y. Ebrahimipour, I. Sheikhshoaie, A. Crochet, M. Khaleghi and K. M. Fromm, *J. Mol. Struct.*, 2014, **1072**, 267.

14 S. Lin, S.-X. Liu, J.-Q. Huang and C.-C. Lin, *J. Chem. Soc., Dalton Trans.*, 2002, 1595.
15 I. Kim, B. Kwak and M. S. Lah, *Inorg. Chim. Acta*, 2001, **317**, 12.
16 Q. Y. Mo, J. G. Deng, Y. Liu, G. D. Huang, Z. W. Li, P. Yu, Y. Gou and F. Yang, *Eur. J. Med. Chem.*, 2018, **156**, 368.
17 D. Sadhukhan, M. Maiti, G. Pilet, A. Bauza, A. Frontera and S. Mitra, *Eur. J. Inorg. Chem.*, 2015, 1958.
18 D. Sadhukhan, M. Maiti, G. Pilet, A. Bauzá, A. Frontera and S. Mitra, *EurJIC*, 2015, **11**, 1958.
19 R. Borah, N. Deori and S. Brahma, *New J. Chem.*, 2020, **44**, 2547.
20 K. Patel, R. N. Patel, Y. Singh, Y. P. Singh, D. Kumhar, R. N. Jadeja, H. Roy, A. K. Patel, N. Patel, N. Patel, A. Banerjee, D. Choquesillo-Lazarte and A. Gutierrez, *Polyhedron*, 2019, **161**, 198.
21 J. R. Macdonald and W. B. Johnson, *Fundamentals of Impedance Spectroscopy*, John Wiley & Sons, Inc., 2018.
22 N. Bonanos, P. Pissis and J. R. Macdonald, John Wiley & Sons, Inc., 2012.
23 J. Ross Macdonald, *Ann. Biomed. Eng.*, 1992, **20**, 289.
24 E. Barsoukov and J. R. Macdonald, *Impedance Spectroscopy: Theory, Experiment, and Applications*, John Wiley & Sons, Inc., 2018.
25 S. Morab, M. M. Sundaram and A. Pivrikas, *Coatings*, 2023, **13**, 1657.
26 U. Guth, Mixed Conductors, Determination of Electronic and Ionic Conductivity (Transport Numbers), in *Encyclopedia of Applied Electrochemistry*, ed. G. Kreysa, K. Ota and R. F. Savinell, Springer, New York, NY, 2014.
27 Y. Xu, Z.-L. Wong and R. Xiao, *Electronic and Ionic Conductivity of Metal-Organic Frameworks in Comprehensive Supramolecular Chemistry II.*, Elsevier, 2017, 7, 399.
28 M. El-Batouti, E. H. Et.-Mossalamy and N. F. At.-Harby, *Asian J. Chem.*, 2015, **27**, 2719.
29 A. Masuya-Suzuki, S. Goto, T. Kambe, R. Karashimada, Y. Kubota and N. Iki, *ChemistryOpen*, 2021, **10**(1), 46.
30 O. I. H. Al-Ajrawy, *J. Vet. Sci.*, 2011, **4**(2), 129.
31 K. S. M. Salih, A. M. Shraim, S. R. Al-Mhini and R. E. Al-Soufi, *Emergent Mater.*, 2021, **4**, 423.
32 I. E. Ifeanyi, J. C. Anyanwu and K. K. Igwe, *Phy. Sci.*, 2020, **5**(2), 145.
33 T.-H. Le, Y. Kim and H. Yoon, *Polymers*, 2017, **9**, 3.
34 Z. Y. Sun, R. Yuan, Y. Q. Chai, L. Xu, X. X. Gan and W. J. Xu, *Anal. Bioanal. Chem.*, 2004, **378**, 490.
35 M. Revanasiddappa, S. Khasim, S. C. Raghavendra, C. Basavaraja, T. Suresh and S. D. Angadi, *E-J. Chem.*, 2008, **5**, 797.
36 K. Q. Ding, Z. B. Jia, Q. F. Wang, N. Tian, R. T. Tong, X. K. Wang and H. B. Chin, *Chem. Lett.*, 2001, 1101.
37 R. S. Joseyphus, E. Viswanathan, C. J. Dhanaraj and J. Joseph, *J. King Saud Univ. Sci.*, 2012, **24**, 233.
38 S. Sarkar, Y. Aydogdu, F. Dagdelen, B. B. Bhaumik and K. Dey, *Mater. Chem. Phys.*, 2004, **88**, 357.
39 J. Sarjanović, M. Stojić, M. Rubčić, L. Pavić and J. Pisk, *Materials*, 2023, **16**(3), 1064.
40 M. Lozano-González, M. E. Sánchez-Vergara, I. Alvarado-Beltrán, M. Leyva-Esqueda, M. Rivera and C. Álvarez-Toledano, *Adv. Mater. Phys. Chem.*, 2017, **7**(2), 70.
41 T. Ghosh, S. Bhattacharya, A. Das, G. Mukherjee and M. G. B. Drew, *Inorg. Chim. Acta*, 2005, **358**, 989.
42 M. Sutradhar, M. V. Kirillova, M. F. C. G. da Silva, L. M. D. R. S. Martins and A. J. L. Pombeiro, *Inorg. Chem.*, 2012, **51**, 11229.
43 V. Vrdoljak, G. Pavlović, T. Hrenar, M. Rubčić, P. Siega, R. Dreos and M. Cindrić, *RSC Adv.*, 2015, **5**, 104870.
44 V. Vrdoljak, T. Hrenar, M. Rubčić, G. Pavlović, T. Friganović and M. Cindrić, *Int. J. Mol. Sci.*, 2023, **24**, 1909.
45 S. N. Choing, A. J. Francis, G. Clendenning, M. S. Schuurman, R. D. Sommer, I. Tamblyn, W. W. Weare and T. Cuk, Long-Lived LMCT in a d0 Vanadium(v) Complex by Internal Conversion to a State of $3d_{xy}$ Character, *J. Phys. Chem. C*, 2015, **119**(30), 17029–17038.
46 D. Patra, N. Biswas, B. Kumari, P. Das, N. Sepay, S. Chatterjee, M. G. B. Drewe and T. Ghosh, *RSC Adv.*, 2015, **2015**(5), 92456.
47 L. A. Dubraja, D. Žilić, K. Olujić, L. Pavić, K. Molčanov and D. Pajić, *New J. Chem.*, 2021, **45**, 6336.
48 J. Meyer, K. Zilberberg, T. Riedl and A. Khan, Electronic structure of vanadium pentoxide: an efficient hole injector for organic electronic materials, *J. Appl. Phys.*, 2011, **110**(033710), 1–5.
49 A. Chakarbarti, K. Hermann, R. Druzinic, M. Witko, F. Wagner and M. Petersen, Geometric and electronic structure of vanadium pentoxide: a density functional bulk and surface study, *Phys. Rev. B: Condens. Matter Mater. Phys.*, 1999, **16**, 10583–10590.
50 *Rigaku Oxford Diffraction. CrysAlisPro Software System, Versions 1.171.42.49, 1.171.41.92a, 1.171.41.93a and 1.171.42.53a*, Rigaku Oxford Diffraction, Oxford, UK, 2020.
51 G. M. Sheldrick, SHELXT-Integrated space-group and crystal-structure determination, *Acta Crystallogr., Sect. A: Found. Adv.*, 2015, 71, 3.
52 G. M. Sheldrick, *Acta Crystallogr., Sect. C: Struct. Chem.*, 2015, **71**, 3.
53 O. V. Dolomanov, L. J. Bourhis, R. J. Gildea, J. A. K. Howard and H. Puschmann, *J. Appl. Cryst.*, 2009, **42**, 339.
54 A. L. Spek, *Acta Crystallogr.*, 2009, **D65**, 148.
55 O. V. Dolomanov, L. J. Bourhis, R. J. Gildea, J. A. K. Howard and H. Puschmann, *J. Appl. Cryst.*, 2009, **42**, 339.